Contents lists available at ScienceDirect

Applied Catalysis B: Environmental

Fast assembly of Ag_3PO_4 nanoparticles within three-dimensional graphene aerogels for efficient photocatalytic oxygen evolution from water splitting under visible light

Can Cui [a,*], Shuang Li [a], Yiwei Qiu [a], Haihua Hu [b], Xiaoyun Li [a], Chaorong Li [a], Junkuo Gao [c], Weihua Tang [d]

[a] Department of Physics and Zhejiang Provincial Key Laboratory of Fiber Materials and Manufacturing Technology, Zhejiang Sci-Tech University, Hangzhou 310018, China
[b] Zhejiang University City College, Hangzhou 310015, China
[c] The Key Laboratory of Advanced Textile Materials and Manufacturing Technology of Ministry of Education, National Engineering Lab for Textile Fiber Materials and Processing Technology (Zhejiang), College of Materials and Textiles, Zhejiang Sci-Tech University, Hangzhou 310018, China
[d] State Key Laboratory of Information Photonics and Optical Communication, Beijing University Posts and Telecommunications, Beijing 100876, China

A R T I C L E   I N F O

A B S T R A C T

Three-dimensional (3D) graphene-based composites have drawn increasing attention in energy applications due to their unique structures and properties. However, the assembly of semiconductor nanoparticles (NPs) in 3D graphene structure is usually a complicated and time-consuming process. Here, we demonstrate a strategy of fast assembling Ag_3PO_4 NPs within 3D graphene aerogels (GAs) with a facile *in situ* ion filtration-precipitation method, in which the sequential filtration of Ag^+ and PO_4^{3-} solutions through the porous 3D graphene structure enables the fast assembly of well-dispersed Ag_3PO_4 NPs throughout the 3D GAs. The 3D GAs not only prevent the agglomeration of Ag_3PO_4 NPs due to the porous and interconnected microstructure but also promote the separation of photo-generated charges in Ag_3PO_4 due to the excellent electrical conductivity of reduced graphene oxide (rGO) that composes 3D GAs. As a result, the 3D Ag_3PO_4/GAs composite shows a considerable enhancement in both the activity and stability in photocatalytic oxygen evolution from water splitting when compared with pristine Ag_3PO_4. In addition to Ag_3PO_4 NPs, the *in situ* ion filtration-precipitation method is also feasible for fast assembling other semiconductor NPs in 3D graphene structures

© 2016 Elsevier B.V. All rights reserved.

1. Introduction

Graphene, a single layer of carbon atoms in a hexagonal lattice, has been regarded as a versatile platform for the fabrication of composite photocatalysts due to its superior electrical conductivity, high specific surface area and high chemical stability [1,2]. Up to now, many graphene-based composite photocatalysts have been synthesized and they exhibited superior photocatalytic performance in water splitting and organic molecules decomposition [1–20]. However, most of the graphene-based composite photocatalysts were prepared by depositing or adsorbing semiconductor NPs on two-dimensional (2D) graphene sheets. Owing to the nanoscale morphology of these particulate graphene-based photocatalysts, it is difficult to carry out successive recycling in practical application. Recently, macroscopic 3D graphene structures constructed by interconnecting 2D graphene sheets have been successfully synthesized by various methods, *e.g.*, self-assembly, template-assisted synthesis, aerosolization, direct deposition, *etc* [21–31]. In addition to the inherent properties of 2D graphene, 3D graphene structure exhibits large accessible surface area, excellent mechanical strength and good flexibility due to its porous and interconnected network structure [21]. The macroscopic porous structure of 3D graphene makes it an easy and convenient recycling support for semiconductor photocatalysts [21–28]. Self-assembly of graphene oxide (GO) sheets is one of the commonly used chemical methods to obtain 3D graphene structures, such as graphene hydrogels (GHs) and GAs. To create 3D graphene based composites, precursor ions are usually added during or after the self-assembly process for *in-situ* growth of semiconductor NPs within 3D graphene structure [21]. Recently, Fan et al. prepared 3D AgX/GAs (X = Br, Cl) composite photocatalyst by *in-situ* depositing AgX NPs in 3D GAs with a successive ionic adsorption and reaction method [22]. However, the additive cetyltrimethylammonium bromide (CTAB) surfactant is not eco-friendly for environment and

---

* Corresponding author.
E-mail addresses: cancui@zstu.edu.cn, msecuican@hotmail.com (C. Cui).

the ionic adsorption requires long time up to 20 h. Liang et al. reported the self-assembly of 3D $AgVO_3$/GAs composite by a one-step hydrothermal method [28], which enables the self-assembly and reduction of GO as well as the formation of $AgVO_3$ NPs simultaneously. However, partial $AgVO_3$ was inevitably reduced into metallic Ag, so the one-step hydrothermal method is not suitable for assembling semiconductor NPs that have weak stability in hydrothermal reduction. Therefore, it is still a challenge to develop facile and mild methods for fast assembly semiconductor NPs in 3D GAs.

Ag_3PO_4 is a promising visible-light-active photocatalyst due to its extremely high efficiency in water splitting and organic molecules decomposition [29–32]. However, the wide application of Ag_3PO_4 is restricted by the inherent drawbacks, including the high recombination rate of photo-generated charges, the weak stability in photocatalysis process as well as the high cost of Ag-containing chemicals [31]. It has been recognized that the combination of graphene sheets with Ag_3PO_4 can promote electron-hole separation and transfer and thus improve the photocatalytic activity and stability of Ag_3PO_4 [12–20]. Even though particulate 2D graphene/Ag_3PO_4 composites have been prepared by various methods [12–20], only very few studies related to 3D graphene/Ag_3PO_4 composite have been reported [33]. Recently, Ma et al. reported the synthesis of graphene/Ag_3PO_4 hydrogel using a common ionic adsorption and reaction method [33]. However, the synthesis process requires long time for ionic adsorption and it is difficult to obtain a homogeneous distribution of Ag_3PO_4 NPs throughout hydrogel without using of any surfactants because the insufficient ionic diffusion in stagnant solution could cause inhomogeneous ion adsorption in the 3D graphene structure.

Here, we demonstrate fast assembly of Ag_3PO_4 NPs in 3D GAs with a facile *in situ* ion filtration-precipitation method. In 3D Ag_3PO_4/GAs composite, nano-sized Ag_3PO_4 are homogeneously anchored on the graphene sheets of 3D GAs, which not only prevents the aggregation of Ag_3PO_4 NPs but also promotes the separation of photo-generated charges by transporting the photo-generated electrons away from Ag_3PO_4. As a result, 3D Ag_3PO_4/GAs exhibits enhanced photocatalytic oxygen evolution rate compared to pristine Ag_3PO_4 in water splitting. The microstructure of the composite and the underlying mechanism for the enhanced photocatalytic performance has been investigated.

2. Experimental

2.1. Materials

All the chemicals were of analytical grade and used without further purification. Silver nitrate ($AgNO_3$), sodium phosphate dibasic dodecahydrate ($Na_2HPO_4 \cdot 12H_2O$), sodium phosphate tribasic (Na_3PO_4) were purchased from Sigma-Aldrich. The deionized water was produced from a Millipore Milli-Q water purification system and used throughout the whole experiments.

2.2. Synthesis of 3D Ag_3PO_4/GAs

Fig. 1 illustrates the synthetic process of 3D Ag_3PO_4/GAs *via* a facile *in situ* ion filtration-precipitation method followed by free-drying. GO was prepared by a modified Hummers method [12]. First, GO aqueous suspension (2 mg/mL) was placed in a Teflon-lined stainless steel autoclave and subjected to hydrothermal treatment at 180 °C for 12 h to generate 3D GHs. Second, 3D GHs cylinder was transferred into a barrel of syringe. 10 mL $AgNO_3$ aqueous solution (0.1 M) was repeatedly injected and passed through the porous 3D GHs cylinder for 5 times to enable the sufficient adsorption of Ag^+ on 3D GHs. The unanchored Ag^+ in 3D GHs/Ag^+

cylinder was removed by washing with deionized water. Then, 10 mL Na_2HPO_4 aqueous solution (0.15 M) was repeatedly injected and passed through the 3D GHs/Ag^+ cylinder for 5 times for the *in situ* precipitation of Ag_3PO_4 NPs through reaction of PO_4^{3-} and Ag^+. Finally, 3D Ag_3PO_4/GHs was washed with deionized water for several times and subsequently subjected to a freeze-drying process to obtain 3D Ag_3PO_4/GAs. Pristine Ag_3PO_4 and a composite of Ag_3PO_4 NPs/2D rGO (Ag_3PO_4/2D rGO) were prepared with conventional precipitation method [12,14] for comparison with 3D Ag_3PO_4/GAs.

2.3. Characterizations

The phase structures of the samples were characterized by X-ray diffraction (XRD) on a Bruker D8 diffractometer using Cu Kα (λ = 1.5406 Å) radiation at 40 kV and 40 mA. Fourier transform infrared (FTIR) spectra were recorded on a Nicolet Avatar 370 spectrometer with powder samples embedded in KBr disks. Raman spectra were measured by a Bruker Raman spectrometer equipped with a 532 nm laser. Scanning electron microscopy was taken on a Zeiss Ultra 55 field emission scanning electron microscope (FESEM, integrated with an EDS/EBSD system) at a voltage of 30 kV. Transmission electron microscopy (TEM) images were conducted using a JEM-2100 microscope at an accelerating voltage of 200 kV. The X-ray photoelectron spectra (XPS) were measured using a Kratos Axis Ultra system with monochromatic Al Kα X-rays (1486.6 eV) operated at 10 mA and 15 kV. The binding energies were calibrated to the C1 s (284.6 eV) peak. The UV–vis diffuse reflectance spectra were obtained on a Hitachi U3900 UV–vis spectrophotometer by using $BaSO_4$ as the matrix. Nitrogen adsorption–desorption isotherm was obtained at 77 K with an F-sorb 3400 micropore analysis system. The photoluminescence (PL) spectra were obtained on a Hitachi F7000 fluorescence spectrophotometer at an excitation wavelength of 290 nm. Time-resolved photoluminescence (PL) spectroscopy were run on an Edinburgh Instruments FLS-920 fluorescence spectrophotometer.

2.4. Photocatalytic performance measurements

The photocatalytic oxygen evolution was performed in Labsolar III system (Beijing Perfectlight Technology Co. Ltd.). An outer irradiation-type photoreactor (Pyrex reaction vessel) was connected to a closed gas circulation and an evacuation system. The evolved gases were analyzed by an online gas chromatograph (GC) equipped with a thermal conductivity detector (TCD) and molecular sieve (5 Å pore size). High purity Ar was used as the carrier gas. In the experiment, 50 mg of photocatalyst was dispersed into 100 mL deionized water containing sacrificial reagent (0.005 M $AgNO_3$). Before reaction, the whole system was pumped out to remove the dissolved air. A 300 W Xe lamp, equipped with a UV cut-off filter and placed 1 cm away from the vessel, was used as the visible light source (λ > 400 nm). A circulation of water through an external cooling coil was conducted to maintain the temperature of suspension at about 25 °C.

2.5. Photoelectrochemical measurements

Photoelectrochemical measurements were performed in a conventional three electrode cell, using a Pt plate and a Ag/AgCl electrode (3 M KCl) as counter electrode and reference electrode, respectively. The working electrodes were prepared by the doctor-blade method on fluorine-doped SnO_2 (FTO) conductive glass. 10 mg photocatalyst powder was mixed with 2 mL ethanol and 2 μL of Nafion solution (5 wt.%) with ultrasonication for 30 min to form slurry. The slurry was then coated onto FTO glass, whose side part was previously protected using Scotch tape, controlling
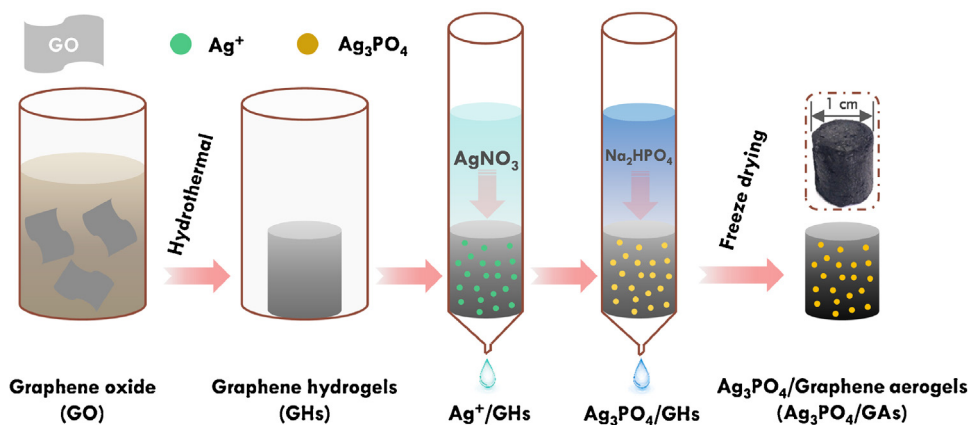
Fig. 1. Schematic illustration of the synthesis process of 3D Ag$_3$PO$_4$/GAs.

the exposed area of the electrode to be 1 cm^2. After air drying, the electrode was heating at 200 °C for 2 h in vacuum to improve adhesion. The electrolyte was a 0.02 M Na$_3$PO$_4$ aqueous solution degassed with N$_2$ for 2 h prior to the measurement. The illumination source was a 150 W Halogen lamp equipped with an UV cut filter ($\lambda > 400$ nm). The transient photocurrent was recorded at a bias voltage of 0.5 V vs. Ag/AgCl. The electrochemical impedance spectroscopy (EIS) measurements were carried out at the open-circuit voltage of the photocatalyst electrode under light illumination with an electrochemical measurement system (Princeton Applied Research, Versa STAT 3).

3. Results and discussion

Fig. 2(a) shows the photograph of 3D GAs prepared from the self-assembly of GO sheets in hydrothermal reduction followed by a freeze-drying process. It has been known that GO sheets can be reduced and self-assembled into 3D GHs during hydrothermal process, and the shape and the volume of 3D GHs can be easily controlled using reactors of various features [21–25,34]. In our experiment, the self-assembly of GO was carried out in a cylindrical autoclave, resulting a 3D GHs cylinder with radius ~1 cm and height ~1 cm. The water content in as-prepared 3D GHs is more than 95% [34]. After freeze-drying, 3D GHs has transferred into 3D GAs, which retains the shape and volume of 3D GHs. It is obvious that the volume of 3D GAs is distinct from that of the thermal-drying product, indicating the porous structure of 3D GAs. Fig. 2(b) shows the XRD patterns of graphite, GO and 3D GAs. The interlayer spacing of 3D GAs is calculated to be 3.76 Å, which is slightly higher than that of graphite (3.36 Å) and much lower than that of GO (7.92 Å), suggesting the presence of residual oxygenous groups on the interconnected graphene sheets of 3D GAs after hydrothermal reduction [34]. Fig. 2(c) and (d) shows the SEM and TEM images of 3D GAs. It is clear that 3D GAs have a well-defined and interconnected 3D porous structure, and the pore walls consist of thin layers of graphene sheets. It has been reported that 3D GAs have high adsorption capacities to metal ions (Ag$^+$, Cd^{2+}, Pb^{2+}, etc.) and cationic dyes due to the large accessible surface area [35–38].

Fig. 3 shows the microstructure of 3D Ag$_3$PO$_4$/GAs composite. It is clear that Ag$_3$PO$_4$ NPs are uniformly distributed throughout the graphene sheet surface of the 3D GAs [Fig. 3(a)–(c)]. The distribution of Ag$_3$PO$_4$ NPs is determinate by the distribution of Ag$^+$ adsorbed on 3D GHs in the synthesis process. Owing to the electrostatic attraction between Ag$^+$ and negative charged oxygenous groups, Ag$^+$ are well dispersed within the interconnected graphene structure when AgNO$_3$ solution passes through 3D GHs. Then, the Ag$^+$ react evenly with the subsequently entered PO$_4{}^{3-}$

and results in a homogeneous in situ growth of Ag$_3$PO$_4$ NPs on the surface of the hierarchical pores of 3D GAs. The Ag$_3$PO$_4$ NPs are 20–50 nm in size [Fig. 3(d)]. The lattice fringes with a d spacing of 0.27 nm in a high resolution TEM image of 3D Ag$_3$PO$_4$/GAs is corresponding to the (210) planes of the body-centered cubic structure of Ag$_3$PO$_4$ [Fig. S1(a)]. This is consistent with the XRD result of 3D Ag$_3$PO$_4$/GAs [Fig. S1(b)], which confirms the co-existence of Ag$_3$PO$_4$ and GAs. It should be noted that, when a similar precipitation method was employed to synthesize pristine Ag$_3$PO$_4$ [Fig. S2(a)] and a composite of Ag$_3$PO$_4$ with 2D rGO (Ag$_3$PO$_4$/2D rGO) [Fig. S2(b)] without using of any surfactants [12,14], the resulting Ag$_3$PO$_4$ particles (submicron in size) are much larger than those in 3D Ag$_3$PO$_4$/GAs, and they agglomerate seriously. To further study the Ag$_3$PO$_4$ distribution in 3D Ag$_3$PO$_4$/GAs, the EDS spectra and the element mapping were measured and shown in Fig. S3. Four elements (C, O, P and Ag) have been detected and the atomic ratio of 1.36: 4.82 for P: Ag is close to the stoichiometry of Ag$_3$PO$_4$ [Fig. S3(a)]. The Ag$_3$PO$_4$ content in 3D Ag$_3$PO$_4$/GAs is about 32.3 wt%. The element mapping images [Figs. S3(b–e)] indicate that the elements of C, O, P and Ag are homogeneously distributed in the selected area of 3D Ag$_3$PO$_4$/GAs [insert of Fig. S3(a)]. This further indicates that 3D GAs can dramatically inhibit the agglomeration of Ag$_3$PO$_4$, resulting in high dispersed Ag$_3$PO$_4$ NPs within 3D GAs. The N$_2$ adsorption–desorption isotherm measurement [Fig. S4] indicates that 3D Ag$_3$PO$_4$/GAs exhibits a typical type IV curve of mesoporous materials. Based on the Barrett–Joyner–Halenda (BJH) equation, the pore size of 3D Ag$_3$PO$_4$/GAs mainly lies in the range of 3–4 nm [inset in Fig. S4]. The Brunauer–Emmett–Teller (BET) specific surface area of 3D Ag$_3$PO$_4$/GAs is 102.5 m^{2}g^{-1}.

Fig. 4(a) and (b) shows the Raman and FTIR spectra of GO, 3D GAs, Ag$_3$PO$_4$ and 3D Ag$_3$PO$_4$/GAs. In the Raman spectra [Fig. 4(a)], two typical Raman peaks (D and G bands) related to graphene materials are observed for GO, 3D GAs and 3D Ag$_3$PO$_4$/GAs. The D band is assigned to edge or in-plane sp^3 defects and disordered carbon, whereas the G band arises from the in-plane vibration of ordered sp^2-bonded carbon atoms in a two-dimensional hexagonal lattice [22,39]. In contrast to GO, the D band shifts from 1363 cm^{-1} to 1345 cm^{-1} and the G band shifts from 1620 cm^{-1} to 1592 cm^{-1} in 3D Ag$_3$PO$_4$/GAs. The shifts of D and G bands are also observed in 3D GAs. Furthermore, higher intensity ratio of D/G is observed in the Raman spectrum of 3D Ag$_3$PO$_4$/GAs ($I_D/I_G = 0.88$) when compared to that of GO ($I_D/I_G = 0.65$). The shifts of Raman peak position and the increase of D/G intensity ratio indicate that GO has been reduced into rGO after hydrothermal reduction [22]. The peaks at 905 and 993 cm^{-1} in the spectrum of pristine Ag$_3$PO$_4$ are ascribed to the terminal oxygen bond vibration in phosphate chains [13,14]. The Raman spectrum of 3D Ag$_3$PO$_4$/GAs can be regarded as a com-
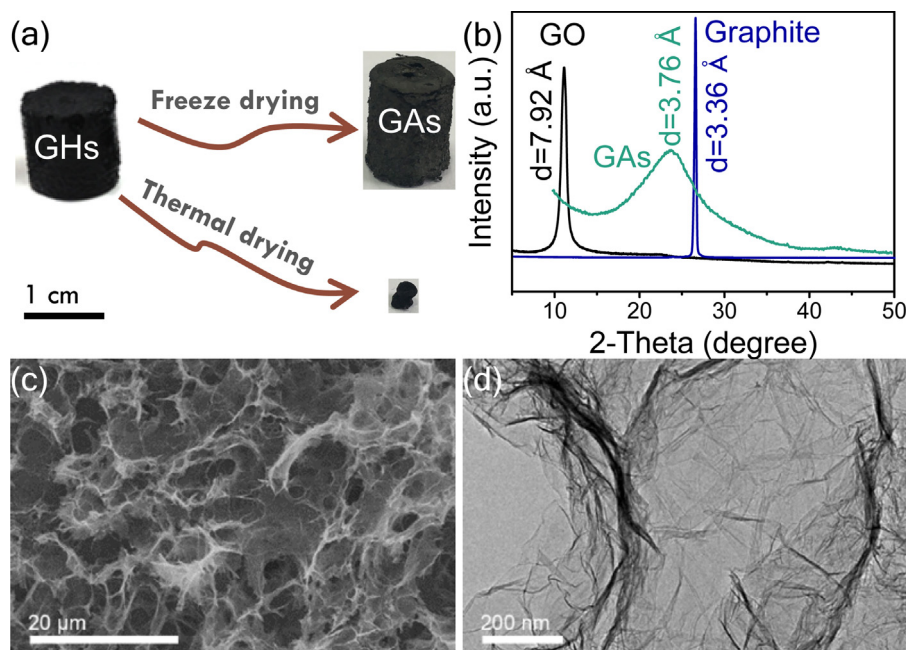
Fig. 2. (a) Photographs of 3D GHs and its dried product after freeze-drying (3D GAs) and thermal-drying. (b) XRD patterns of graphite, GO and 3D GAs. (c) SEM and (d) TEM images of 3D GAs.

bination of 3D GAs spectrum and Ag_3PO_4 spectrum with slight blue shifts in peak positions, which may be due to the interaction between rGO sheets and Ag_3PO_4 [39,40]. The similar results are also revealed in the FTIR spectra [Fig. 4(b)]. The IR peaks of C—OH ($1391\,cm^{-1}$) and alkoxy C—O—C ($1100\,cm^{-1}$) in 3D Ag_3PO_4/GAs shift to higher wavenumbers compared to those of 3D GAs due to the charge interaction between Ag_3PO_4 and GAs [14]. Additionally, the peak intensity of C=O and alkoxy C—OH decreases significantly in the spectra of 3D GAs and 3D Ag_3PO_4/GAs due to the reduction of GO into rGO. It is suggested that the high pressure and temperature in hydrothermal process can partially remove the oxygenated functional groups in GO by breaking the bonds between the carbon and oxygenous groups [21].

The chemical composition and valence state of C and Ag in 3D Ag_3PO_4/GAs was studied with XPS spectra, as shown in Figs. 4 and S5. The XPS survey spectrum [Fig. S5(a)] confirms the co-existence of C, O, P and Ag in 3D Ag_3PO_4/GAs. The high resolution spectrum of C 1s [Fig. 4(c)] can be simply divided into three peaks at around 284.8, 286.2 and 288.6 eV, which are respectively attributed to binding energies of sp^2 hybridized non-oxygenated ring carbon atoms (C—C), oxygen-containing epoxy/hydroxyl groups (C—O) and carboxyl (OC—=O) [38–42]. In comparison with the C 1s XPS spectrum of GO [Fig. S5(b)], the absence of C=O peak as well as the significant decrease of C—O and O—C=O peaks in 3D Ag_3PO_4/GAs is ascribed to the reduction of GO into rGO. Fig. 4(d) shows the XPS spectrum of Ag 3d. The binding energies of Ag $3d_{5/2}$ and Ag $3d_{3/2}$ are 368.6 and 374.6 eV, which are typical values for Ag^+ in Ag_3PO_4
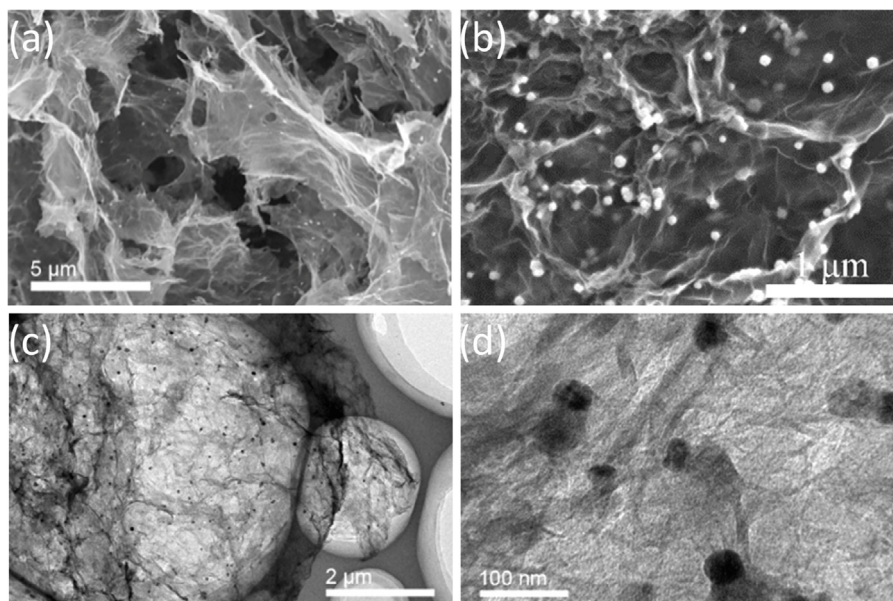

Fig. 3. (a, b) SEM and (c, d) TEM images of 3D Ag_3PO_4/GAs.

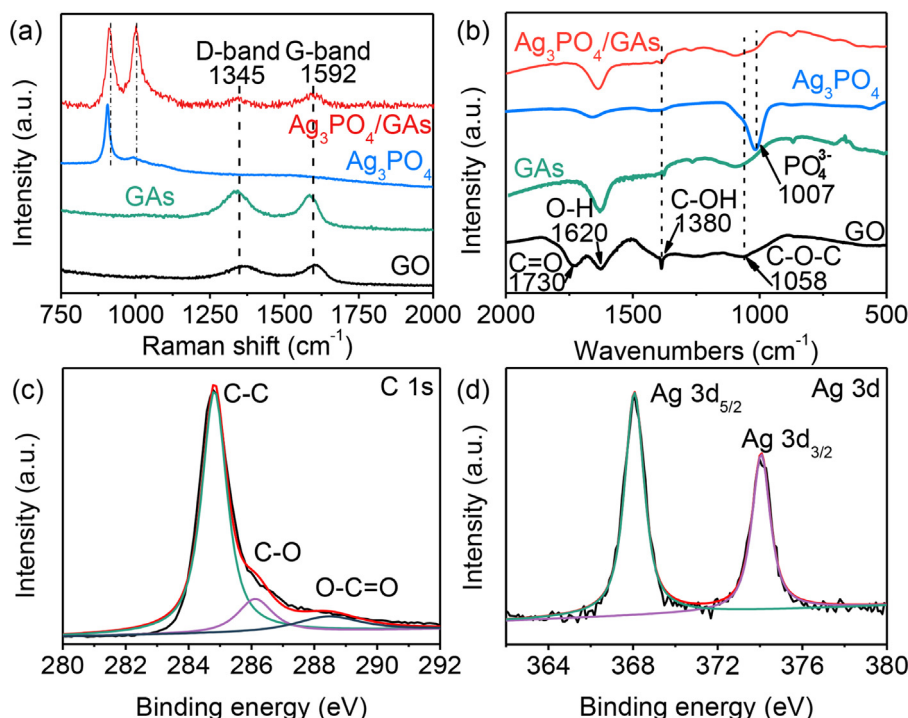**Fig. 4.** (a) Raman and (b) FTIR spectra of GO, 3D GAs, Ag_3PO_4 and 3D Ag_3PO_4/GAs. XPS spectra of (c) C 1s and (d) Ag 3d of 3D Ag_3PO_4/GAs.
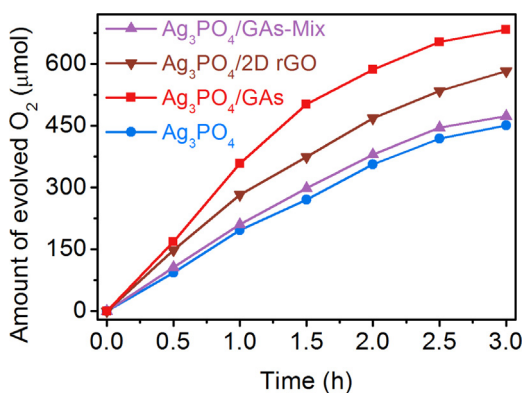

Fig. 5. Photocatalytic oxygen evolution under visible light irradiation from 0.005 M aqueous $AgNO_3$ solution over pristine Ag_3PO_4, Ag_3PO_4/GAs-Mix, Ag_3PO_4/2D rGO and 3D Ag_3PO_4/GAs.

Table 1
Comparison of 3D Ag_3PO_4/GAs with others particulate Ag_3PO_4-based photocatalysts in O_2 evolution under visible light. $C_{catalyst}$ is the concentration of photocatalyst in solution.

Photocatalyst	Enhancement	Light source	$C_{catalyst}$ $(mg\,mL^{-1})$	Ref.
Ag_3PO_4/$SrTiO_3$	36%	300 W	1.11	[44]
Ag_3PO_4/WO_3	27%	300 W	3	[45]
Ag_3PO_4/C_3N_4	46%	LED	3	[46]
3D Ag_3PO_4/GAs	40%	300 W	0.5	This work

[43]. No additional XPS peaks related to metallic Ag^0 are found in 3D Ag_3PO_4/GAs. Fig. S6 (a) shows the UV–vis diffuse reflection spectrum of 3D Ag_3PO_4/GAs. The pristine Ag_3PO_4 and Ag_3PO_4/2D rGO prepared with conventional precipitation method are also measured for comparison. All the samples show clear absorbance edge at wavelength of about 530 nm, which is corresponding to the band-gap absorption of Ag_3PO_4 [29]. The improved light absorbance in wavelength above 530 nm in 3D Ag_3PO_4/GAs and Ag_3PO_4/2D rGO is ascribed to the incorporation of GAs and rGO. The absorbance of 3D Ag_3PO_4/GAs is slightly higher than that of Ag_3PO_4/2D rGO due to the light trapping ability of 3D graphene structure.

The photocatalytic performance of 3D Ag_3PO_4/GAs was evaluated by oxygen evolution from water splitting in $AgNO_3$ aqueous solution under visible-light irradiation [Fig. 5]. Here, $AgNO_3$ is used as a sacrificial reagent [29]. For pristine Ag_3PO_4, 480 μmol O_2 has been evolved in 3 h. A slight increasing of O_2 evolution is observed for mechanical mixing of Ag_3PO_4 and GAs (Ag_3PO_4/GAs-Mix), which has the same Ag_3PO_4 content as 3D Ag_3PO_4/GAs. The chemically precipitated Ag_3PO_4/2D rGO [12,14] with simi-

lar Ag_3PO_4 content exhibits higher photocatalytic O_2 evolution activity than Ag_3PO_4/GAs-Mix but lower photocatalytic activity than 3D Ag_3PO_4/GAs. The O_2 evolution over 3D Ag_3PO_4/GAs is 675 μmol (4860 μmol h^{-1} g^{-1}) in 3 h, enhanced by 40% in comparison with that of pristine Ag_3PO_4. Since 3D GAs has no activity for O_2 evolution and the Ag_3PO_4 content in 3D Ag_3PO_4/GAs is equal to that in Ag_3PO_4/GAs-Mix and Ag_3PO_4/2D rGO and much lower than that of pristine Ag_3PO_4, the superior photocatalytic activity of 3D Ag_3PO_4/GAs can be ascribed to the size effect of Ag_3PO_4 as well as the tight contact of Ag_3PO_4 NPs with rGO sheets of 3D GAs. In Table 1, the photocatalytic activity of 3D Ag_3PO_4/GAs is compared with those of other particulate Ag_3PO_4-based composites reported previously [44–46]. Taking into account the different experimental conditions, the photocatalytic performance of the composites is demonstrated by the enhancement compared to pristine Ag_3PO_4 in O_2 evolution under visible light. Obviously, 3D Ag_3PO_4/GAs demonstrates outstanding activity among these Ag_3PO_4-based photocatalysts.

Photocurrent response, EIS spectra, PL spectra and time-resolved PL spectra were studied to understand the photo-induced charges generation, separation and transfer as well as the stability of 3D Ag_3PO_4/GAs under light irradiation. Fig. 6(a) shows the photocurrent response of 3D Ag_3PO_4/GAs and Ag_3PO_4 electrodes under visible light irradiation. The Ag_3PO_4 electrode displays photocurrent density of about 1.5 μA cm^{-2} at the beginning of light irradiation. However, the photocurrent density decreases dramat-
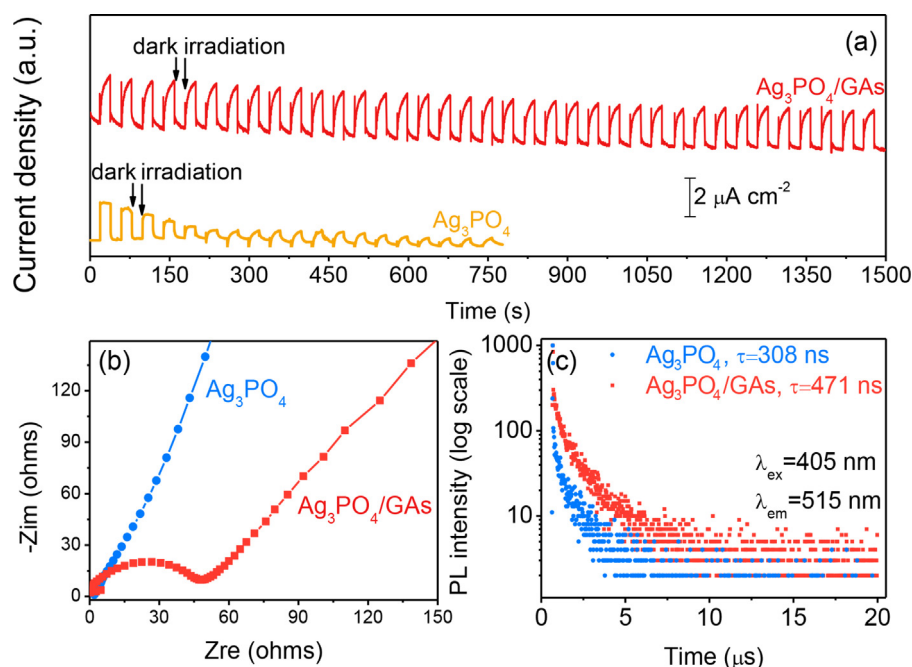
Fig. 6. (a) The periodic on/off photocurrent density response and (b) EIS spectra of Ag_3PO_4 and 3D Ag_3PO_4/GAs electrodes under visible light irradiation ($\lambda > 400$ nm) at 0.5 V bias potential *vs.* Ag/AgCl. (c) Time-resolved PL decay spectra of Ag_3PO_4 and 3D Ag_3PO_4/GAs.

ically with the extension of irradiation, indicative of weak stability of Ag_3PO_4 in photoelectrochemical measurement. The weak stability of Ag_3PO_4 is ascribed to the reduction of lattice Ag^+ into metallic Ag by photo-generated electrons in photo-excited Ag_3PO_4 [29]. In contrast, 3D Ag_3PO_4/GAs exhibits a constant photocurrent density of about 2.5 μA cm^{-2} during 25 min light irradiation, indicative of higher photoelectric conversion efficiency and higher stability of 3D Ag_3PO_4/GAs than pristine Ag_3PO_4. Fig. 6(b) shows the EIS results of Ag_3PO_4 and 3D Ag_3PO_4/GAs electrodes. The 3D Ag_3PO_4/GAs electrode exhibits a much lower resistance than the pristine Ag_3PO_4 electrode, owing to the highly conductive GAs that facilitates electron transfer from anchored Ag_3PO_4 in the whole electrode. The PL spectra in Fig. S6(b) demonstrates that the PL emission of Ag_3PO_4 at about 515 nm in 3D Ag_3PO_4/GAs has been significantly quenched and is even lower than that of Ag_3PO_4/2D rGO due to the fast and efficient electron transfer from nano-sized Ag_3PO_4 to GAs. The above conclusions are further confirmed by the

time-resolved PL spectrum of 3D Ag_3PO_4/GAs [Fig. 6(c)]. The decay time (t) of photo-generated carries can be modeled as follow [47]:

$$1/t = W_0 + W_B \exp(-E_A/kT)$$

where W_0 is the decay rate at temperature T=0, W_B is the rate constant of the trap, and E_A is the activation energy of non-radiative trap states. By fitting the decay data with this model, the average decay lifetime of charge carriers in 3D Ag_3PO_4/GAs is 471 ns, much higher than that in pristine Ag_3PO_4 (308 ns). The greatly extended lifetime of charge carriers further indicates fast charges separation and low recombination in 3D Ag_3PO_4/GAs.

Based on the above experimental results, the photo-induced charges generation, separation and transfer in the water splitting process and the photoelectrochemical process are proposed and schematically illustrated in Fig. 7. Under visible light irradiation, electrons at the valence band (VB) of Ag_3PO_4 are excited into the conduction band (CB) and leave holes at the VB. In the water splitting process, the photo-generated holes at VB of Ag_3PO_4 can oxidize H_2O to evolve O_2 because the potential of the VB of Ag_3PO_4 (2.81 eV *vs.* NHE) [29] is more negative than the O_2 evolution potential
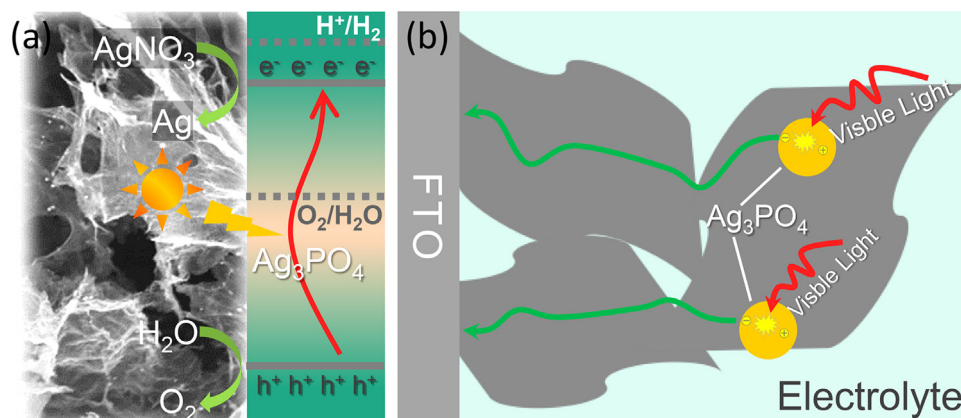

Fig. 7. Schematic illustration of (a) photocatalytic enhancement mechanism of 3D Ag_3PO_4/GAs in oxygen evolution from water splitting in $AgNO_3$ aqueous solution under visible-light irradiation and (b) photo-generated electron transport in 3D Ag_3PO_4/GAs electrode.

(2.23 eV *vs.* NHE) [Fig. 7(a)], while the electrons can be transfer to 3D GAs and reduce Ag^+ (in $AgNO_3$ solution) into metallic Ag. The improved photocatalytic activity of 3D Ag_3PO_4/GAs compared to pristine Ag_3PO_4, Ag_3PO_4/GAs-Mix and Ag_3PO_4/2D rGO can be ascribed to the following reasons: (1) the porous 3D GAs have inhibited the agglomeration of Ag_3PO_4 NPs during the synthesis of 3D Ag_3PO_4/GAs, which provides more active sites than pristine Ag_3PO_4, Ag_3PO_4/GAs-Mix and Ag_3PO_4/2D rGO for the photocatalytic reaction; (2) the nano-sized Ag_3PO_4 enables fast migration of charges towards the surface; (3) 3D GAs provide electrical conductive channels for anchored Ag_3PO_4 NPs, so that electrons are shuttled efficiently from photo-excited Ag_3PO_4 to GAs and increase hole lifetimes leading to efficient water photo-oxidation [31]; (4) the 3D porous structure of GAs enables facile access of Ag^+ electron scavengers ($AgNO_3$ solution) to the entire internal surface of 3D Ag_3PO_4/GAs. Fig. 7(b) schematically illustrates the photogenerated electron transport in 3D Ag_3PO_4/GAs electrode during photoelectrochemical process. The excellent conductivity of rGO sheets and the tight contact between Ag_3PO_4 and rGO promote the photo-generated charge separation and transfer in the electrode. Therefore, the porous 3D Ag_3PO_4/GAs electrode compromises the merits of good photo-generated charge separation and transfer as well as large electrode/electrolyte contact area in the photo-conversion process, leading to dramatically enhanced photocurrent density and stability.

In addition, 3D AgBr/GAs composite has also been prepared *via* the same *in situ* filtration-precipitation method without using of any surfactants. Fig. S7 shows the SEM image of the as-prepared 3D AgBr/GAs, which exhibits a similar microstructure as the previous reported composite fabricated with the assistant of CTAB surfactant [14]. The AgBr NPs are homogeneously distributed within the 3D GAs. This indicates the generality of the *in situ* filtration-precipitation method for fast assembling semiconductor NPs in 3D graphene structures.

4. Conclusions

In summary, we demonstrate a strategy of fast assembling Ag_3PO_4 NPs in the porous structure of 3D GAs with a facile *in situ* ion filtration-precipitation method. The Ag_3PO_4 NPs of 20–50 nm in size are homogeneously distributed within 3D GAs. 3D Ag_3PO_4/GAs shows 40% enhancement in photocatalytic oxygen evolution from water splitting when compared with pristine Ag_3PO_4. 3D Ag_3PO_4/GAs electrode also demonstrates higher and more stable photocurrent response than pristine Ag_3PO_4 electrode in photoelectrochemical measurement. It is concluded that the interconnected structure of 3D GAs facilitates the deposition of well dispersed Ag_3PO_4 NPs and provides more sites for photocatalytic reaction. Furthermore, the tight contact of Ag_3PO_4 NPs with rGO sheets and the excellent electrical conductivity of 3D GAs promote the photo-generated charges separation and transport and thus enhance the photocatalytic activity and stability of 3D Ag_3PO_4/GAs. The synthesis of 3D AgBr/GAs shows the *in situ* ion filtration-precipitation method is feasible for constructing other 3D GAs-based composites.

Acknowledgements

Appendix A. Supplementary data

Supplementary data associated with this article can be found, in the online version, at http://dx.doi.org/10.1016/j.apcatb.2016.07.056.

References

[1] G. Xie, K. Zhang, B. Guo, Q. Liu, L. Fang, J. Gong, Adv. Mater. 25 (2014) 3820–3839.
[2] N. Zhang, M.Q. Yang, S. Liu, Y. Sun, Y.J. Xu, Chem. Rev. 115 (2015) 10307–10377.
[3] C. Xu, J. Zhu, R. Yuan, X. Fu, Carbon 96 (2016) 394–402.
[4] Q. Xiang, J. Yu, M. Jaroniec, J. Am. Chem. Soc. 134 (2012) 6575–6578.
[5] Q. Li, X. Li, S. Wageh, A.A. Al-Ghamdi, J. Yu, Adv. Energy Mater. 5 (2015) 1–28.
[6] R. Bera, S. Kundu, A. Patra, ACS Appl. Mater. Interface 7 (2015) 13251–13259.
[7] M. Zhou, J. Li, Z. Ye, C. Ma, H. Wang, P. Huo, W. Shi, Y. Yan, ACS Appl. Mater. Interface 7 (2015) 28231–28243.
[8] B. Weng, M.Q. Yang, N. Zhang, Y.J. Xu, J. Mater. Chem. A 2 (2014) 9380–9389.
[9] H. Sun, S. Liu, S. Liu, S. Wang, Appl. Catal. B: Environ. 146 (2014) 162–168.
[10] G. Chen, F. Li, Z. Huang, C.Y. Guo, H. Qiao, X. Qiu, Z. Wang, W. Jiang, G. Yuan, Catal. Commun. 59 (2015) 140–144.
[11] Y. Wang, W. Wang, H. Mao, Y. Lu, J. Lu, J. Huang, Z. Ye, B. Lu, ACS Appl. Mater. Interface 6 (2014) 12698–12706.
[12] C. Cui, Y. Wang, D. Liang, W. Cui, H. Hu, B. Lu, S. Xu, X. Li, C. Wang, Y. Yang, Appl. Catal. B: Environ. 158–159 (2014) 150–160.
[13] Q. Xiang, D. Lang, T. Shen, F. Liu, Appl. Catal. B: Environ. 162 (2015) 196–203.
[14] X. Yang, H. Cui, Y. Li, J. Qin, R. Zhang, H. Tang, ACS Catal. 3 (2013) 363–369.
[15] A. Samal, D.P. Das, K.K. Nanda, B.K. Mishra, J. Das, A. Dash, Chem. Asian J. 11 (2016) 584–595.
[16] X. Fan, J. Shao, Z. Li, F. Ma, A. Meng, Q. Li, New J. Chem. 40 (2016) 1330–1335.
[17] X. Yang, J. Qin, Y. Jiang, K. Chen, X. Yan, D. Zhang, R. Li, H. Tang, Appl. Catal. B: Environ. 166–167 (2015) 231–240.
[18] X. Yang, J. Qin, Y. Jiang, R. Li, Y. Li, H. Tang, RSC Adv. 4 (2014) 18627.
[19] H. Cui, X. Yang, Q. Gao, H. Liu, Y. Li, H. Tang, R. Zhang, J. Qin, X. Yan, Mater. Lett. 93 (2013) 28–31.
[20] C. Cui, Y. Qiu, H. Hu, N. Ma, S. Li, L. Xu, C. Li, J. Xu, W. Tang, RSC Adv. 6 (2016) 43697.
[21] S. Mao, G. Lu, J. Chen, Nanoscale 7 (2015) 6924–6943.
[22] Y. Fan, W. Ma, D. Han, S. Gan, X. Dong, L. Niu, Adv. Mater. 27 (2015) 3767–3773.
[23] Y. Zhou, C.H. Yen, S. Fu, G. Yang, C. Zhu, D. Du, P.C. Wo, X. Cheng, J. Yang, C.M. Wai, Y. Lin, Green Chem. 17 (2015) 3552–3560.
[24] B. Qiu, M. Xing, J. Zhang, J. Am. Chem. Soc. 136 (2014) 5852–5855.
[25] Z.S. Wu, S. Yang, Y. Sun, K. Parvez, X. Feng, K. Müllen, J. Am. Chem. Soc. 134 (2012) 9082–9085.
[26] L. Fan, B. Li, D.W. Rooney, N. Zhang, K. Sun, Chem. Commun. 51 (2015) 1597–1600.
[27] Z. Tong, D. Yang, J. Shi, Y. Nan, Y. Sun, Z. Jiang, ACS Appl. Mater. Interface 7 (2015) 25693–25701.
[28] L. Liang, Y. Xu, Y. Lei, H. Liu, Nanoscale 6 (2014) 3536–3539.
[29] Z. Yi, J. Ye, N. Kikugawa, T. Kako, S. Ouyang, H. Stuart-Williams, H. Yang, J. Cao, W. Luo, Z. Li, Y. Liu, R.L. Withers, Nat. Mater. 9 (2010) 559–564.
[30] Y. Bi, S. Ouyang, N. Umezawa, J. Cao, J. Ye, J. Am. Chem. Soc. 133 (2011) 6490–6492.
[31] D.J. Matin, G. Liu, S.J. Moniz, Y. Bi, A.M. Beate, J. Ye, J. Tang, Chem. Soc. Rev. 44 (2015) 7808–7828.
[32] X. Yang, H. Tang, J. Xu, M. Antonietti, M. Shalom, ChemSusChem 8 (2015) 1350–1358.
[33] J. Ma, C. Chen, F. Yu, New J. Chem. 40 (2016) 3208.
[34] Y. Xu, K. Sheng, C. Li, G. Shi, ACS Nano 4 (2010) 4324–4330.
[35] Y. Shen, Q. Fang, B. Chen, Environ. Sci. Technol. 49 (2015) 67–84.
[36] Z. Sui, Q. Meng, X. Zhang, R. Ma, B. Cao, J. Mater. Chem. 22 (2012) 8767–8771.
[37] H. Gao, Y. Sun, J. Zhou, R. Xu, H. Duan, ACS Appl. Mater. Interface 5 (2013) 425–432.
[38] X. Zhang, D. Liu, L. Yang, L. Zhou, T. You, J. Mater. Chem. A 3 (2015) 10031–10037.
[39] G. Zhao, L. Jiang, Y. He, J. Li, H. Dong, X. Wang, W. Hu, Adv. Mater. 23 (2011) 3959–3963.
[40] Q. Li, B. Guo, J. Yu, J. Ran, B. Zhang, H. Yan, J.R. Gong, J. Am. Chem. Soc. 133 (2011) 10878–10884.
[41] Z. Wang, L. Yin, M. Zhang, G. Zhou, H. Fei, H. Shi, H. Dai, J. Mater. Sci. 49 (2014) 1585–1593.
[42] Q. Li, B. Guo, J. Yu, J. Ran, B. Zhang, H. Yan, J.R. Gong, J. Am. Chem. Soc. 13 (2011) 10878–10884.
[43] H. Yu, Y. Yu, J. Liu, P. Ma, Y. Wang, F. Zhang, Z. Fu, J. Mater. Chem. A 3 (2015) 19439–19444.
[44] X. Guan, L. Guo, ACS Catal. 4 (2014) 3020–3026.
[45] Y. Chang, K. Yu, C. Zhang, R. Li, P. Zhao, L.L. Lou, S. Liu, Appl. Catal. B: Environ. 176 (2015) 363–373.
[46] X. Yang, Z. Chen, J. Xu, H. Tang, K. Chen, Y. Jiang, ACS Appl. Mater. Inteface 7 (2015) 15285–15293.
[47] R. Li, S. Yerci, L. Dal Negro, Appl. Phys. Lett. 95 (2009) 041111.